

AD _____

Award Number: DAMD17-01-1-0330

TITLE: Image-Guided Surgery of Primary Breast Cancer Using
Ultrasound Phased Arrays

PRINCIPAL INVESTIGATOR: Emad S. Ebbini, Ph.D.

CONTRACTING ORGANIZATION: University of Minnesota
Minneapolis, Minnesota 55455-2070

REPORT DATE: July 2004

TYPE OF REPORT: Annual

PREPARED FOR: U.S. Army Medical Research and Materiel Command
Fort Detrick, Maryland 21702-5012

DISTRIBUTION STATEMENT: Approved for Public Release;
Distribution Unlimited

The views, opinions and/or findings contained in this report are those of the author(s) and should not be construed as an official Department of the Army position, policy or decision unless so designated by other documentation.

20050715 117

REPORT DOCUMENTATION PAGEForm Approved
OMB No. 074-0188

Public reporting burden for this collection of information is estimated to average 1 hour per response, including the time for reviewing instructions, searching existing data sources, gathering and maintaining the data needed, and completing and reviewing this collection of information. Send comments regarding this burden estimate or any other aspect of this collection of information, including suggestions for reducing this burden to Washington Headquarters Services, Directorate for Information Operations and Reports, 1215 Jefferson Davis Highway, Suite 1204, Arlington, VA 22202-4302, and to the Office of Management and Budget, Paperwork Reduction Project (0704-0188), Washington, DC 20503

1. AGENCY USE ONLY (Leave blank)		2. REPORT DATE July 2004	3. REPORT TYPE AND DATES COVERED Annual (1 Jul 03 - 30 Jun 04)	
4. TITLE AND SUBTITLE Image-Guided Surgery of Primary Breast Cancer Using Ultrasound Phased Arrays			5. FUNDING NUMBERS DAMD17-01-1-0330	
6. AUTHOR(S) Emad S. Ebbini, Ph.D.				
7. PERFORMING ORGANIZATION NAME(S) AND ADDRESS(ES) University of Minnesota Minneapolis, Minnesota 55455-2070 E-Mail: emad@ece.umn.edu			8. PERFORMING ORGANIZATION REPORT NUMBER	
9. SPONSORING / MONITORING AGENCY NAME(S) AND ADDRESS(ES) U.S. Army Medical Research and Materiel Command Fort Detrick, Maryland 21702-5012			10. SPONSORING / MONITORING AGENCY REPORT NUMBER	
11. SUPPLEMENTARY NOTES				
12a. DISTRIBUTION / AVAILABILITY STATEMENT Approved for Public Release; Distribution Unlimited				12b. DISTRIBUTION CODE
13. ABSTRACT (Maximum 200 Words) No abstract provided.				
14. SUBJECT TERMS No subject terms provided.				15. NUMBER OF PAGES 20
				16. PRICE CODE
17. SECURITY CLASSIFICATION OF REPORT Unclassified	18. SECURITY CLASSIFICATION OF THIS PAGE Unclassified	19. SECURITY CLASSIFICATION OF ABSTRACT Unclassified	20. LIMITATION OF ABSTRACT Unlimited	

NSN 7540-01-280-5500

Standard Form 298 (Rev. 2-89)
Prescribed by ANSI Std. Z39-18
298-102

Table of Contents

Cover.....	1
SF 298.....	2
Table of Contents.....	3
Introduction.....	4
Body.....	4
Key Research Accomplishments.....	7
Reportable Outcomes.....	7
Conclusions.....	8
References.....	8
Appendices.....	8

Introduction

High-intensity focus ultrasound (HIFU) is gaining wider acceptance in noninvasive or minimally invasive targeting of abnormal tissues (e.g. cancer) for destruction. Piezocomposite transducer technology, especially for phased arrays, is providing high-quality HIFU applicators with increased bandwidth and reduced parasitic cross coupling between the array elements. In addition to increasing the efficacy of HIFU applicators, these technological enhancements allow for the use of HIFU arrays in imaging the target region before, after, and intermittently during lesion formation. This leads to a unique paradigm of image-guided surgery with HIFU in which the coordinate systems for both therapy and imaging are inherently registered. This project investigates the feasibility of using piezocomposite phased arrays as dual-mode ultrasound array (DMUA) applicators for the noninvasive treatment of primary breast cancers. Both therapeutic and imaging capabilities of the dual-mode arrays are investigated leading to a real-time dual-mode array system to be used in pursuing *in vivo* animal experiments in the future.

During the last three years, we have demonstrated the lesion formation and imaging capabilities of the DMUA. This includes an experimental verification of one of the most important advantages of DMUA applicators for noninvasive surgery. Specifically, we have demonstrated the feasibility of image-based feedback for refocusing in the presence of strongly scattering critical targets, e.g. major blood vessels or ribs or bony structures. This work, which was presented at the International Symposium on Biomedical Imaging (ISBI'04) as an invited paper, demonstrates the unique advantage of DMUA applicators over other forms of guidance. Unfortunately, significant fraction of the elements of the new 64-element prototype malfunctioned in the last few months and the array performance has become unstable, especially in heating applications. We have been in touch with the manufacturer (Imasonic, Besancon, France) to try to find out the reasons for the malfunction. We are currently awaiting a new quote for a replacement prototype. In the mean time, we have requested a one-time no-cost extension till June 30, 2005. While this report indicates that practically all the subtasks have been completed, the overall demonstration of a real-time lesion formation under image guidance is yet to be done. This is what we hope to accomplish during the extension.

Body

This report is structured in accordance with the approved statement of work (SoW). In what follows, we give the tasks and subtasks of the approved SoW with each subtask followed directly by what has been accomplished with respect to it. For the subtasks planned for years 2 and 3 of the grant period, they are given here for completeness, but no comments follow these subtasks.

Task 1. Thresholds for Thermal Ablation of Breast and Fatty Tissue (Months 1 – 12):

- a) *Investigation of the intensity/exposure threshold curve; lesion size and characterization of damage (1 – 3):* Completed (Year 1 Report)
- b) *Imaging of discrete thermal lesions with therapeutic arrays (1 – 3):* Completed (Year 1 Report).
- c) *Long-duration volumetric ablation of porcine fatty tissue (3 – 9):* Completed (Year 1 Report).
- d) *Imaging of volumetric ablations using the therapeutic array and diagnostic scanners (3 – 12):* Completed (Year 2 Report).

Task 2. Treatment Planning and Optimization of Volumetric Ablation with Phased Arrays in Fatty Tissue (Months 6 – 24):

- a) *Thermal modeling based on bioheat equation and Saparato and Dewey thermal dose integral for damage: Discrete lesions (6 – 12):* Completed (Year 1 Report)
- b) *Thermal modeling for multiple lesions with variable levels of proximity and cooling time between shots (12 – 18):* Completed (Year 2 Report).
- c) *Optimization of multiple-focus phased array patterns for simultaneous placement multiple discrete lesions (12 – 24):* Completed. Simulation study results are consistent with our previous publications and expectations stated in Year 2 Report. The current DMUA prototype is capable of producing up to 4 high-quality foci simultaneously. This should help reduce the treatment time for volumetric lesions by a factor of 4 for a conventional raster of focal points is used.

Task 3. Detection and Localization of Cavitation Activity During Thermal Lesion Formation in Breast and Fatty Tissue (Months 1 – 24):

- a) *Detection of subharmonic activity in single-channel and beamformed data (1 – 12):* Completed (Year 1 Report).
- b) *Localization of cavitation from beamforming of multiple receiving channels (12 – 24):* We have the electronics and the systems ready to perform this task. However, due to the malfunction of significant fraction of array elements, we are hesitant to drive the DMUA prototype at high level to produce cavitation in tissue. We are confident that we will be able to test this goal once the new DMUA is received.
- c) *Localization using time-frequency and related methods (6 – 18):* Completed (Year 2 Report)

Task 4. Image Characterization of Thermal Lesions in Breast and Fatty Tissue (Months 1 – 24)

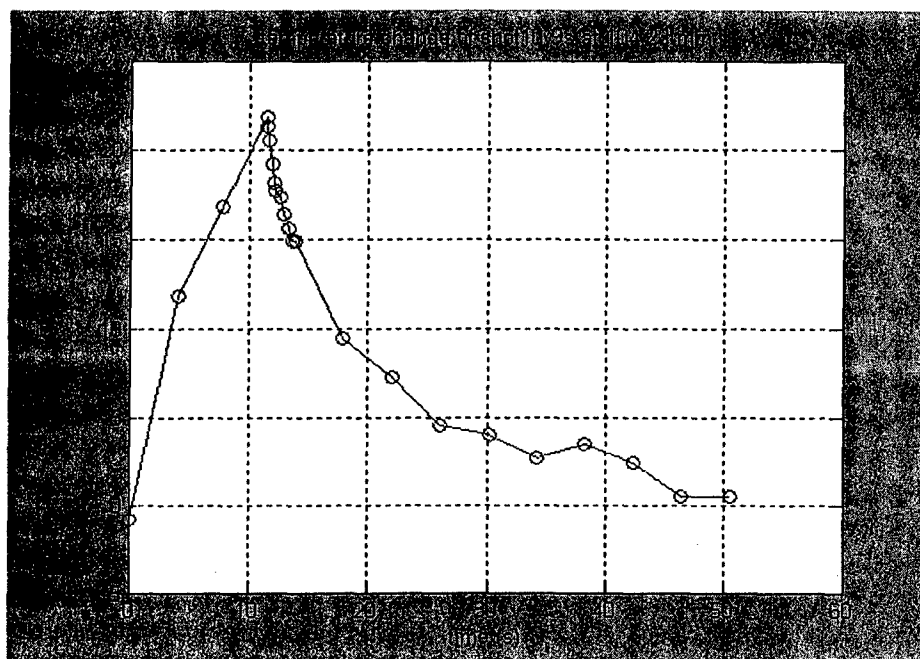
- a) *Characterization of grayscale images for discrete thermal lesions (1 – 6):* Completed (Year 1 Report).
- b) *Characterization of tissue dependent parameters (1 – 12):* Completed (Year 1 Report: (Expected) negative results).
- c) *Characterization of second harmonic imaging (12 – 24):* Completed (Year 2 Report).
- d) *Correlation of imaging parameters with histologic characterization of tissue ablations (12 – 24):* This is currently ongoing work. We have requested the addition of Dr. Robert Griffin from the Department of Therapeutic Radiology as an investigator on this project to help with this task beginning the 3rd year of the project. .

Task 5. Image-based Adaptive Refocusing of Therapeutic Arrays in Inhomogeneous Fatty Tissue (Months 12 – 24)

- a) *Focusing with reference to natural specular targets (12 – 18):* Completed (Year 2 Report).
- b) *Temperature feedback (12 – 24):* Completed (See Task 6 subtask d).
- c) *Discrete thermal lesions as beacons (12 – 24):* RF data from single-shot lesions in porcine liver were analyzed and all normal lesion data sets clearly showed a strong localized echo from the near boundary of the lesion that can be reliably used for focusing. We believe that we can further refine this idea by creating extremely small lesions amounting to point reflectors. Consequently, the quality of focusing can be significantly improved.

Task 6. Real-time Dual-mode Phased Array System for Volumetric Thermal Ablation of Breast and Fatty Tissue (Months 1 – 36)

- a) Design and fabrication of 64-channel receive system (1 – 12): A 64-channel diplexer circuit allowing the use of each array element in transmit and receive has been fabricated and tested. In addition, 8-to-1 multiplexer boards were designed and fabricated to allow data collection from 8 receiving elements on one analog-to-digital converter (A/D). This will reduce the hardware cost of the system without severely compromising the real-time nature of image data collection. Please see d) below for an example of how this new receiver system was used.
- b) Design and fabrication of transmit/receive control circuitry (1 – 18): Completed (Year 1 Report).
- c) DSP-based real-time beamformer (12 – 30): We have identified a VXI based real-time controller for beamforming. This controller will be sufficiently fast to perform real-time beamforming and uploading of image data to the controller workstation. The acquisition and testing of this controller is delayed due to the difficulties with the current DMUA prototype. This work will be performed during the extension period.
- d) Experimental testing, calibration, and characterization of imaging system (24 - 36): Real-time data collection from 8 channels to a single A/D has been demonstrated during a 9-second heating experiment. Not only were we able to demonstrate beamforming but we were also able to extract temperature rise from the focus location. The figure below shows the estimated temperature change near the geometric focus of the dual-mode array (at 100 mm) due to the 9-second heating pulse from the same array. The open circles indicate the instants when the data was collected for temperature calculations. As can be seen from the figure, noninvasive temperature estimates were made at 3 and 6 seconds during heating. The heating pulse was interrupted for 100 ms for data collection for each measurement point. This includes the communications time for the controlling computer. If a real-time operating system were used, it would have taken less than 2 milliseconds to collect the imaging data for temperature calculation. The acquisition time can be reduced further if we dedicate more A/Ds on the receiver side, i.e. one per 4 receiving elements instead of 1 per 8.



Key Research Accomplishments

- First one-to-one comparison of imaging performance of a dual-mode array with a diagnostic transducer (Appendix I).
- First real-time data collection for noninvasive temperature calculation. Will be reported in future meetings.
- First demonstration of image-based feedback for refocusing the array in the presence of strongly scattering target (Appendix II).

Reportable Outcomes

- Phukpattaranont, P.; Ebbini, E.S., "Post-beamforming second-order Volterra filter for pulse-echo ultrasonic imaging," *IEEE Trans. on Ultrasonics, Ferroelectrics, and Frequency Control*, vol. 50(8), pp. 987-1001, Aug. 2003.
- Yao and Ebbini, "Imaging with Large-Aperture Arrays with Heterogeneous Directive Elements," *Proc. 2003 IEEE Ultrasonics Symposium*, vol., pp. 1243 - 1246.
- Yao and Ebbini, "Real-time Monitoring of the Transients of HIFU-induced Lesions," *Proc. 2003 IEEE Ultrasonics Symposium*, vol., pp. 1006 - 1009.
- Yao and Ebbini, "Dual-mode Ultrasound Phased Arrays for Imaging and Therapy," *Special Session on Advanced Methods in Ultrasound Imaging, ISBI 2004, Arlington, VA, April 2004 (Invited Paper)*.
- Invited paper at the 147th Meeting of the Acoustical Society of America in New York, NY, May 24 - 28, 2004 (abstract entitled Monitoring of HIFU-induced Lesions Using Active Imaging Methods by Hui and Ebbini).
- Yao and Ebbini, "Refocusing of Dual-mode arrays in the presence of strongly scattering objects," *Proc. 2004 IEEE Ultrasonics Symposium*, to appear.
- Yao and Ebbini, "Noninvasive Localized Ultrasonic Measurement of Tissue Properties," *Proc. 2004 IEEE Ultrasonics Symposium*, to appear.

Conclusions

After characterizing and optimizing the imaging capabilities of the DMUA prototype in year 2, we have experimentally demonstrated one of the most important advantages of these arrays in noninvasive surgery. Namely, we have demonstrated the feasibility of using image-based feedback to refocus DMUAs in the presence of strongly scattering targets. We have also begun the investigation of quantitative imaging of HIFU-induced lesions through active imaging methods. Specifically, we are developing techniques for measuring local absorption, perfusion, and elastic properties of HIFU-induced lesions. We are developing these techniques using both diagnostic scanners and our DMUA prototypes. This work was reported at the Acoustical Society and at the IEEE Ultrasonics Symposium in May and August of 2004. More complete reports on this work will be developed soon (This is actually the Ph.D. thesis of Ms. Yao who is the lead graduate student working on this project.)

References

- [Ebbini:91] E. Ebbini and C. Cain, "A spherical-section ultrasound phased array applicator for deep localized hyperthermia," *IEEE Trans. Biomed. Eng.*, vol. 38, pp. 634-643, 1991.
- [Seip:95a] R. Seip and E. Ebbini, "Non-invasive estimation of tissue temperature response to heating fields using diagnostic ultrasound," *IEEE Trans. Biomed. Eng.*, vol. 42, no. 8, pp. 828-839, August 1995.
- [Seip:95b] R. Seip, P. VanBaren, C. Simon, and E. Ebbini, "Non-invasive spatio-temporal temperature change estimation using diagnostic ultrasound," in *IEEE Ultrason. Symp.*, pp.1613-1616, November 1995.
- [Seip:96a] R. Seip, *Feedback for Ultrasound Thermotherapy*, PhD thesis, EECS, University of Michigan, February 1996.
- [Seip:96b] R. Seip, P. VanBaren, C. Cain, and E. Ebbini, "Non-invasive real-time multipoint temperature control for ultrasound phased array treatments," *IEEE Trans. Ultrason., Ferroelec., Freq. Contr.*, vol. 43, no. 6, pp.1063-1073, November 1996.
- [Simon:98c] C. Simon, P. VanBaren, and E. Ebbini, "Two-dimensional temperature estimation using diagnostic ultrasound," *IEEE Trans. Ultrason. Ferroelec., Freq. Contr.*, vol. 45, no. 4, pp. 1088-1099, July 1998.

Appendices

- I. Yao and Ebbini, "Imaging with Large-Aperture Arrays with Heterogeneous Directive Elements," Proc. 2003 IEEE Ultrasonics Symposium, vol., pp. 1243 - 1246.
- II. Yao and Ebbini, "Dual-mode Ultrasound Phased Arrays for Imaging and Therapy," Special Session on Advanced Methods in Ultrasound Imaging, ISBI 2004, Arlington, VA, April 2004.
- III. Yao and Ebbini, "Real-Time Monitoring of the Transients of HIFU-Induced Lesions."

IMAGING WITH LARGE-APERTURE ARRAYS WITH HETEROGENEOUS DIRECTIVE ELEMENTS

Hui Yao and Emad S. Ebbini

Department of Electrical and Computer Engineering
University of Minnesota, Minneapolis, MN 55455

Abstract – We have developed a new imaging algorithm for optimization of the contrast resolution of large-aperture arrays utilizing directive elements with heterogeneous responses. The algorithm employs depth-dependant pre- and post-beamforming filtering to optimize the SNR of the echo data throughout the imaging field. Sub-aperture processing is also employed to maximize the coherence of the echo data, both with respect to tissue aberrations and element heterogeneity. Pre-beamforming and sub-aperture processing lead to significant reduction in imaging artifacts due to reverberations, a significant degradation factor due to the need for water standoff. Images of quality assurance phantoms as well as *ex-vivo* liver tissue were obtained using our concave (100 mm radius of curvature) 64-element 1 MHz dual-mode array (DMA) and a commercial scanner. The results show that the DMA has a 50 dB field-of-view (FOV) centered at its geometric focus. This FOV extends by 6 cm and 4 cm in the axial and lateral directions, respectively. In addition, the spatial and contrast resolutions of this DMA have been tested using wire targets and speckle cell size calculations and found to be consistent with the transducer bandwidth and aperture size.

I. INTRODUCTION

Recently, non-invasive and minimally invasive thermal surgeries have become widely accepted in clinics and hospitals worldwide. Reliable imaging techniques for aiming, monitoring and visualization can help clinics gradually accept non-invasive and minimally invasive thermal surgeries. Image guidance methods based on MRI [1], CT [2] and ultrasound [3] have been proposed.

Most of the image guidance systems, including some ultrasound systems, have separate image guidance sub-system and therapeutic sub-system. The advent of piezocomposite transducer technology has made it feasible to design and fabricate dual-mode arrays capable of high-power therapeutic delivery while having a wide enough bandwidth for pulse-echo operation. One such DMA has been described and introduced in our previous reports [3]. The main advantage of this approach is the inherent registration between the therapeutic and imaging coordinate systems. Previously, we have shown that our 64-element concave (100 mm ROC) is capable of producing lesions in freshly excised *ex vivo* tissue. This same array was also used to obtain before and after

images of the lesion location. Echogenicity from the lesion location typically increased with significant increase in nonlinear echo components, probably due to the presence of microbubbles. We have shown that post-beamforming nonlinear imaging techniques have increased the contrast and spatial resolution of the lesion echogenicity leading to more accurate lesion maps. This effort is ongoing and provides a significant motivation towards the continued development of DMAs.

However, at this point, DMAs must be optimized primarily for therapeutic delivery based on the depth and the size of the target (e.g. liver tumors with partial obstruction by the rib cage.) This typically leads to an imaging array with elements that are too directive to provide a uniform FOV in the treatment region and its surrounding. Furthermore, the use of the array elements in high-power applications results in some degradation over time that may affect the imaging performance of those elements. This degradation typically leads to heterogeneity in the array elements that may significantly degrade the array performance. Finally, the DMA's typically large, geometrically-focused aperture introduces significant image artifacts due to reverberation components with delays well into the FOV. These tend to distort the speckle and produce a recognizable artifacts near the geometric focus. Such artifacts must be removed from the element data (pre-beamforming) or they may render the beamformed image useless. These limitations must be studied and accounted for in order to optimize the image quality of DMAs for potential use as self-guided systems for surgical applications.

II. THEORY

A. Synthetic Aperture Imaging

Images were obtained using a full synthetic aperture technique [4]. The image pixel at coordinates (x_p, z_p) was therefore computed by [5]:

$$I(x_p, z_p) = \sum_{i=1}^{64} \sum_{j=1}^{64} A_i \cdot B_j \cdot s_{i,j} [(R_{ip} + R_{jp})/c], \quad (1)$$

where i is the transmit element index, j is the receive element index, A_i is the transmit apodization weight at element i , B_j is the receive apodization weight at element j , R_{ip} and R_{jp} are the distance from the transmit and receive element,

respectively, from the image pixel, c is the speed of sound in the medium being imaged, and $s_{i,j}(t)$ is the echo acquired where transmitting with element i and receiving with element j . Specialized image reconstruction programs were written to evaluate the intensity at (x_p, z_p) .

B. Single-Transmit Imaging

The synthetic aperture imaging algorithm described above can be used to produce the higher quality conventional images than can be expected from a given array. However, due to the fact that transmit beams are synthesized by superposition of single-element transmit patterns, the nonlinear interactions of the real-time transmit beams cannot be accounted for using the imaging algorithms. Therefore, we have modified our 64-channel phased array driver to allow for pulsed transmission on all 64 channels simultaneously. This allowed us to use the full power of the transmit beams and, therefore, observe their nonlinear interactions with the tissue media. The image formation process due to a single transmit focused beam is a modified version of Eq. (1) as follows:

$$I(x_p, z_p) = \sum_{j=1}^{64} B_j \cdot s_{i,j}[(R_0 + R_{jp})/c], \quad (2)$$

where $s_j(t)$ is the received waveform at element j due to the transmitted beam and R_0 is a fixed distance determined by the focal depth of the transmit beam. All other quantities in Eq.(2) are the same as their counterparts in Eq. (1).

C. Special Considerations

In conventional phased-array beamforming, grating-lobe levels are determined by the array pattern as well as the element directivity. Both of these factors are important in DMAs as the array elements typically have high directivity.

1) *Array Gain Compensation (GC) Algorithm:* The intensity gain is defined as the peak field intensity in W/cm^2 divided by the average W/cm^2 output from the array at a set of field locations. In order to correctly calculate the contrast ratio of the image in a speckle region, gain compensation is required. Since the array is dynamically focused on both transmit and receive, 2-way compensation is utilized.

2) *Element Directivity (ED) Algorithm:* Accounting for element directivity in the beamforming algorithm reduces the grating lobes and, consequently, improves the dynamic range. Furthermore, accounting for element directivity affects the SNR of the resulting image. Figure 1 shows the main lobes of two array elements. Point A, B and C are three points within the DMA's FOV. Clearly the SNR of the beamformed signals at these pixel locations due to these two elements will not be the same. In this illustration, the SNR at pixel B will be the highest among the three while pixel C has the lowest SNR. Taking the element directivities into account improves the SNR throughout the imaging FOV. The

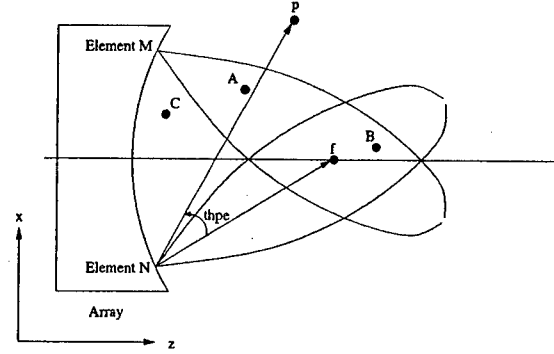


Figure 1: Element directivity patterns in the FOV of our concave DMA.

element directivity weight function is:

$$\theta = \frac{\sin[kw \sin(\theta_{thpe})/2]}{kw \sin(\theta_{thpe})/2} \quad (3)$$

where $k = \frac{2\pi}{\lambda}$, λ is the wavelength, w is the element width, θ_{thpe} is shown in Figure 1. For point P, the larger the θ_{pe} , the smaller the weight is, the lower the SNR near that pixel due to the receiving (or transmitting) element.

3) *Reverberations:* Almost all imaging arrays have a region in the immediate vicinity of the transducer that cannot be used for imaging, usually referred to as the dead zone. This is due to reverberating electrical signals and potentially some surface waves that mix with the acoustical echoes from the near field of the transducer. In the case of DMAs, the large aperture produces reverberating signals (and potentially surface waves) with significant delays that strongly interfere with acoustical echoes from the imaging volume. Furthermore, due to the concave nature of most DMAs, these object-independent signals produce strong interference near the geometric center of the array. A solution for this problem is to remove these signals from the element data before beamforming. Receive signals are first recorded in pure water for all the transmit patterns of interest. These signals are subtracted from the receive element data from the imaging target for the same transmit patterns. Fortunately, we have been able to demonstrate the validity of this approach with our array data. Unless stated otherwise, all the results shown below employ this compensation scheme.

III. SETUP

A. Experiment Setup

Figure 2 demonstrates the image acquisition model. A 64-element concave linear phased array (LPA) is used for the image acquisition. The array can be connected to a 64-channel driver that can operate in CW therapeutic mode or pulsed imaging mode. It can also be connected to a standard pulser receiver. Synthetic aperture images were obtained

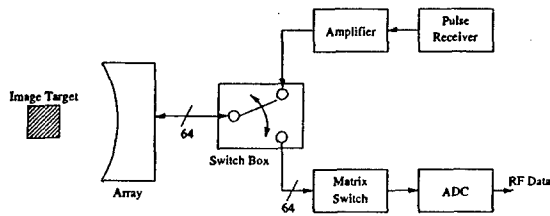


Figure 2: image experiment setup

TABLE I
SPECIFICATIONS OF THE DMA AND COMMERCIAL CA 421 PROBE

parameters	DMA	CA 421 probe
Center frequency (MHz)	1	3.2
Type	concave LPA	convex array
Pitch (mm)	2	0.306
Number of elements	64	192
Elevation (mm)	100	12
Radius (mm)	100	40
Mechanical focus (mm)	100	80

with the latter approach while single transmit images were obtained with the 64-channel transmitter.

A modified Technos MPX system from ESAOTE, Genoa, Italy is used to acquire images to compare with the images from the DMA. The system is modified to allow the upload of high-quality beamformed RF data from the Technos system to computer. A CA 421 convex abdominal probe is used to acquire images from the same target as the DMA. The images from CA 421 probe were acquired in B-mode with a single-cycle transmit pulse with center frequency 3 MHz. Table I summarizes the parameters of the DMA and the CA 421 probe.

B. Assessment of Image Quality

1) *Contrast Ratio*: The contrast ratio (CR) is used for comparison of contrast between the test object and the background materials inside the image. CR is defined in (4)[6]:

$$CR = 10 * \log_{10}(I_1/I_2); \quad (4)$$

where I_1 and I_2 are the average intensity of the test object and the background materials.

2) *Resolution Measurement*: Correlation lengths calculated from the 2D autocorrelation of echoes in images from speckle target are used to measure spatial resolution [7]. Uniform speckle regions from the test object area were identified to compute the average speckle correlation cell size

$$S_c = \int_{-x}^x \int_{-y}^y \frac{C_I(x, y)}{C_I(0, 0)} dx dy, \quad (5)$$

where $C_I(x, y)$ is the 2D correlation function of the intensity autocovariance function. X and Y are chosen to be large

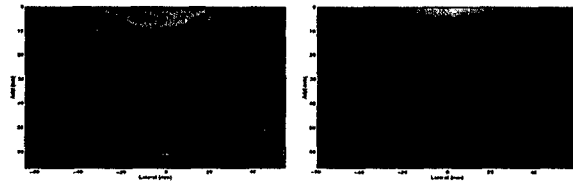


Figure 3: Images (50 dB) of the multi-tissue CIRS Model 40 phantom. Left: Technos CA 421 probe. Right: DMA.

enough to allow the magnitude of the autocovariance to drop to a negligible levels. The vertical and horizontal correlation cell sizes, representing the axial and lateral resolution, are used to compare spatial resolution of the DMA and the CA421 abdominal probe available on the Technos MPX.

IV. RESULTS

3) *Multi-Tissue Phantom*: Figure 3 shows 50-dB images of the CIRS Model 40 multi-tissue phantom obtained using the Technos CA421 probe (left) and the DMA. The result shows that the wire targets register correctly on both images. For the DMA, however, some of the wire targets farthest from the geometric center are barely visible. The smallest ± 15 dB contrast targets (< 4 mm) are practically invisible on the DMA image. Contrast targets with diameters 6 mm or larger and contrast of ± 15 dB can be detected, but are dominated by specular reflections for both positive and negative contrast targets.

4) *3D Contrast Phantom*: Figure 4(a) shows the array intensity gain calculated in a region corresponding to the image shown to the right. Figure 4 (b) and (c) are obtained from the DMA without and with array gain compensation, respectively. Contrast ratios determined from image of DMA (with gain compensation) and the image from the CA 421 probe are shown in Table II. In Table II, "+" means with this algorithm, "-" means without this algorithm. S_a is the vertical correlation cell size and S_l is the horizontal correlational cell size. Table II show the ED algorithm improves the SNR of images from 1.70 to 1.75 in the central area. GC algorithm improves the contrast ratio of the images from 3.32 dB to 8.95 dB (the ideal value is 9 dB). Compared with the CA 421 probe, the DMA has better lateral correlation cell size but poor axial correlation cell size. This is consistent with the low $f_{\#}$ of the array and its limited bandwidth.

A. Images of Wire Targets

Figure 5 is the result of applying element directivity algorithm (described in Section II-C.2) to wire target image. Figure ?? is the post beamform result without applying the element directivity. Figure ?? is the post beamform result applying the element directivity. Figure 5 shows the element directivity algorithm reduce grating-lobe artifacts and, therefore, extends the size of the FOV.

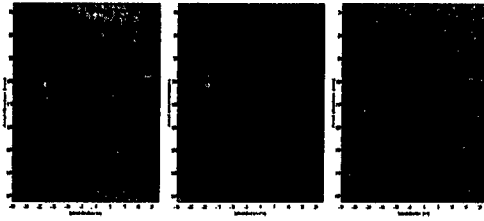


Figure 4: Images (50 dB) from the CIRS Model 55 3D contrast phantom. Left: DMA w/o GC; Center: DMA w/ GC; Right: Technos.

TABLE II
IMAGE QUALITY CHARACTERISTICS OF THE EGG PHANTOM

parameters	CR (dB)	SNR	S_I (mm)	S_a (mm)
Ideal value	9	1.9	N/A	N/A
CA421	9.12	2.32	3	0.98
+GC-ED	8.95	1.70	0.8	2.9
+GC+ED	8.33	1.75	0.8	2.9
-GC-ED	3.32	1.89	0.8	2.9
-GC+ED	2.15	1.90	0.8	2.9

B. Synthetic Aperture Image vs Single-Transmit Image

Images of a freshly excised and degassed porcine liver sample in a tissue holder are displayed in Figure 6. They are obtained with the full synthetic aperture technique described in Section II-A and the single-transmit technique described in Section II-B. This result demonstrates the usefulness of the STF data in direction of the transmit focus. In fact, the quality of the speckle signal along the transmit focus is equivalent to that obtained using full synthetic-aperture imaging. Some geometric distortion can be observed off-axis.

V. CONCLUSIONS

Characterization of the image quality from the DMA demonstrates the feasibility of using this array in image-guided surgical applications. The spatial and contrast resolutions of this array, while not sufficient for high-quality diagnostic applications, are consistent with the bandwidth

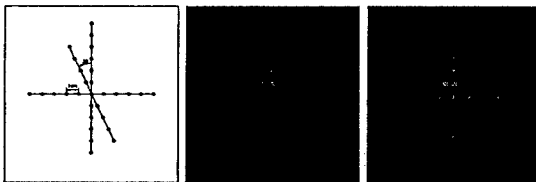


Figure 5: Images (50 dB) of wire target array without (center) and with (right) element directivity.

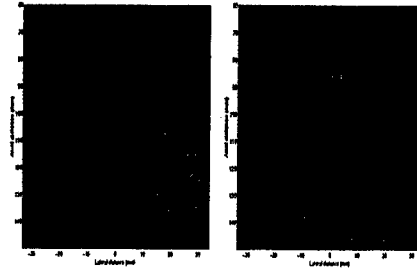


Figure 6: Images (50 dB) of a freshly excised porcine liver sample obtained using full SA (left) and STF modes.

and geometry of the array. Furthermore, the speckle components of the beamformed data is suitable for relevant signal processing algorithms such as displacement tracking and temperature estimation.

ACKNOWLEDGMENTS

Funded by Grant DAMD17-01-1-0330 US Army Medical Research and Materiel Command. Thanks for Pornchai Phukpattaranont for help with various aspects of this paper.

VI. REFERENCES

- [1] J. Poorter, C. Wagter, Y. Deene, C. Thomsen, and F. Stahlberg, "Noninvasive mri thermometry with the proton resonance frequency (prf) method: In vivo results in human muscle," *Magn.Reson.Mde.*, vol. 33, pp. 74-81, 1995.
- [2] P. Meaney, K. Paulsen, A. Hartov, and R. Crane, "Initial in vivo experience with eit as a thermal estimator during hyperthermia," *Ultrasound Med.Biol.*, vol. 12, pp. 573-591, 1996.
- [3] Emad S Ebbini, "Combined ultrasound surgery with ultrasound phased arrays," *SPIE Bios: Surgical Applications of Energy*, 1998.
- [4] K. Thomenius, "Evolution of ultrasound beamformers," in *1996 IEEE ultrasonics symposium*, 1996, pp. 1615-1622.
- [5] H.Yao, P.Phukpattaranont, and E.S.Ebbini, "Enhanced lesion visualization in image-guided noninvasive surgery with ultrasound phased arrays," in *Proc. of the 23rd Annual Int. Conf. of the IEEE*, 2001, vol. 3, pp. 2492-2495.
- [6] W.K.Pratt, *Digital Image Processing*, A Wiley-Interscience Publication, 1978.
- [7] R.F. Wagner, M.F. Berg, A. Insana, and S.W. Smith, "Fundamental correlation lengths of coherent speckle in medical ultrasound images," *ultrasonics, Ferroelectrics and Frequency Control, IEEE transaction*, vol. 35, pp. 34-44, Jan. 1988.

APPENDIX 2

DUAL-MODE ULTRASOUND PHASED ARRAYS FOR IMAGING AND THERAPY

Hui Yao and Emad S. Ebbini

Department of Electrical and Computer Engineering
University of Minnesota, Minneapolis, MN 55455

Abstract — We have recently demonstrated the imaging capabilities of a prototype 64-element 1 MHz concave array with 100 mm radius of curvature. This array was optimized for therapeutic applications using high-intensity focused ultrasound (HIFU). We have shown that this dual-mode ultrasound array (DMUA) has a therapeutic operating field (*ThxOF*) that extends by ± 3 cm and ± 2 cm around its geometric center in the axial and lateral directions, respectively. We have also shown that appropriate apodization and accounting for element directivity along with conventional synthetic aperture beamforming produce a 50 dB imaging field of view (*LxFOV*) larger than the *ThxOF*. In addition, the spatial registration of imaging targets is as accurate as commercially available scanners. In this paper, we present results from an image-based refocusing algorithm whereby images formed by the DMUA are used to identify a refocusing target and a set of critical points where the incident power is to be minimized. The algorithm is validated experimentally in tissue mimicking phantom with strongly scattering ribs placed between the DMUA and the target. These results demonstrate what is potentially the most powerful advantage of the use of DMUAs in image-guided surgery. Namely, the inherent registration between the imaging and therapeutic coordinate systems. This allows for direct definition of targets and any surrounding critical structures to be avoided to minimize the collateral damage. With these capabilities, DMUAs may provide a most powerful paradigm for image-guided surgery.

I. INTRODUCTION

Recently, non-invasive and minimally invasive thermal surgeries have become widely accepted in clinics and hospitals worldwide. Reliable imaging techniques for aiming, monitoring and visualization can help clinics gradually accept non-invasive and minimally invasive thermal surgeries. Image guidance methods based on MRI [1], CT [2] and ultrasound [3] have been recently proposed.

Most of the image guidance systems, including some ultrasound systems, have separate image guidance sub-system and therapeutic sub-system. The advent of piezocomposite transducer technology has made it feasible to design and fabricate dual-mode arrays capable of high-power therapeutic delivery while having a wide enough bandwidth for pulse-echo operation. One such DMUA has been described and introduced in our previous reports (e.g. [3]). The *ThxOF* for this prototype was experimentally shown to match the theoretically predicted profile based on array and element directivity analysis [3]. Furthermore, the *LxFOV* was also

shown to extend beyond the *ThxOF* for this prototype [4].

The main advantage of this approach is the inherent registration between the therapeutic and imaging coordinate systems. Once the real-time imaging capability is available for DMUAs, one can envision a treatment paradigm in which the HIFU beam is guided in real-time based on imaging of the treatment field by the same transducer. The doctor only needs to locate the target on the image and the system automatically generates the amplitude and phase distribution to focus the HIFU pulse at the desired target. In addition, it is possible to define additional points in the treatment field where the incident power is to be minimized to reduce or eliminate collateral damage, e.g. to nearby bone structures. In this paper, we present the first experimental verification of an image-based refocusing algorithm employing images from the DMUA prototype to identify the refocusing target as well as a number of critical structures to be avoided. One obvious application of this capability is targeting tumors in the liver that are partially obstructed by the ribcage [5]. This capability is unique to DMUAs due to the inherent registration between the imaging and therapeutic coordinate systems.

II. THEORY

A. Synthetic Aperture (SA) Imaging

Images were obtained using a full synthetic aperture technique [6]. The image pixel at coordinates (x_p, z_p) was therefore computed by [3]:

$$I(x_p, z_p) = \sum_{i=1}^{64} \sum_{j=1}^{64} A_i \cdot B_j \cdot s_{i,j}[(R_{ip} + R_{jp})/c], \quad (1)$$

where i is the transmit element index, j is the receive element index, A_i is the transmit apodization weight at element i , B_j is the receive apodization weight at element j , R_{ip} and R_{jp} are the distance from the transmit and receive element, respectively, from the image pixel, c is the speed of sound in the medium being imaged, and $s_{i,j}(t)$ is the echo acquired where transmitting with element i and receiving with element j . Specialized image reconstruction programs were written to evaluate the intensity at (x_p, z_p) .

B. Single-Transmit Focus (STF) Imaging

The synthetic aperture imaging algorithm described above can be used to produce higher quality conventional images

than can be expected from a given array. However, due to the fact that transmit beams are synthesized by superposition of single-element transmit patterns, the nonlinear interactions of the real-time transmit beams cannot be accounted for using the imaging algorithms. Therefore, we have modified our 64-channel phased array driver to allow for pulsed transmission on all 64 channels simultaneously. This allowed us to use the full power of the transmit beams and, therefore, observe their nonlinear interactions with the tissue media. The image formation process due to a single transmit focused beam is a modified version of Eq. (1) as follows:

$$I(x_p, z_p) = \sum_{j=1}^{64} B_j \cdot s_j[(R_0 + R_{jp})/c], \quad (2)$$

where $s_j(t)$ is the received waveform at element j due to the transmitted beam and R_0 is a fixed distance determined by the focal depth of the transmit beam. All other quantities in Eq.(2) are the same as their counterparts in Eq. (1).

C. Special Considerations

In conventional phased-array beamforming, grating-lobe levels are determined by the array pattern as well as the element directivity. Both of these factors are important in DMUAs as the array elements typically have high directivity.

1) *Array Gain Compensation (GC) Algorithm:* The intensity gain is defined as the peak field intensity in W/cm^2 divided by the average W/cm^2 output from the array at a set of field locations. In order to correctly calculate the contrast ratio of the image in a speckle region, gain compensation is required. Since the array is dynamically focused on both transmit and receive, 2-way compensation is utilized.

2) *Element Directivity (ED) Algorithm:* Accounting for element directivity in the beamforming algorithm reduces the grating lobes and, consequently, improves the dynamic range. Furthermore, accounting for element directivity affects the SNR of the resulting image. The element directivity weight function is:

$$D(\theta_{pe}) = \frac{\sin[kw \sin(\theta_{pe})/2]}{kw \sin(\theta_{pe})/2} \quad (3)$$

where $k = \frac{2\pi}{\lambda}$, λ is the wavelength, w is the element width, θ_{pe} is the angle between the axis of the radiating (receiving) element and the vector from the element center to the pixel.

D. Refocusing in the Presence of Obstacles

Assume we have an N -element array with arbitrary, but known, geometry radiating into a homogeneous half space. The objective is to maximize the array intensity gain at a target point \vec{r}_T while minimizing the incident power at a set of critical points, $\vec{r}_C(i)$, $i = 1, 2, \dots, M_C$. This is an optimization problem that can be solved using Lagrange multipliers or a regularized minimum-norm least squares solution as follows [5]:

- Let the raw vector $\mathbf{h} = [h_1(\vec{r}_T), h_2(\vec{r}_T), \dots, h_N(\vec{r}_T)]$ be the array directivity vector at \vec{r}_T (note that $h_k(\vec{r}_T)$ is the directivity of the k th element at \vec{r}_T).
- Form the matrix \mathbf{H}_C from the raw vectors $\mathbf{h}_i = [h_1(\vec{r}_C(i)), h_2(\vec{r}_C(i)), \dots, h_N(\vec{r}_C(i))]$.
- Form the weighting matrix, $\mathbf{W}_C = (\mathbf{H}_C \mathbf{H}_C^* + \gamma \mathbf{I})^{-1}$ where \mathbf{I} is the identity matrix and γ is an appropriately chosen regularization parameter.
- The optimal complex array driving vector is given by $\mathbf{u} = \mathbf{W}_C \mathbf{h}_T^* (\mathbf{h}_T^* \mathbf{W}_C \mathbf{h}_T^*)^{-1}$.

Both the target and the critical points can be derived from images formed by the DMUA in synthetic aperture or in single-transmit focus modes. This is probably the most powerful feature of the use of the DMUA in image-guided applications.

III. EXPERIMENT SETUP

Figure 1 (left) shows the image acquisition model. A 64-element concave linear phased array is used for the image acquisition. The array can be connected to a 64-channel driver that can operate in CW therapeutic mode or pulsed imaging mode. It can also be connected to a standard pulser receiver through a matrix switch. Synthetic aperture images were obtained with the latter approach while single transmit images were obtained with the 64-channel transmitter. Figure 1 (right) shows a schematic of the DMUA with an imaging target containing three strongly scattering ribs on top of a tissue-mimicking phantom containing a strong scatterer near the geometric center of the DMUA. The target is a thermocouple wire 0.1 mm in diameter and the ribs are plastic bars with diameter of 8 mm. They are positioned in a plane just over 40 mm from the vertex of the DMUA with approximate spacing of 20 mm between them.

A modified Technos MPX system from ESAOTE, Genoa, Italy is used to acquire images for comparison with images of the same target from the DMUA. The system is modified to allow the upload of high-quality beamformed RF data from the Technos system to computer. A CA 421 convex abdominal probe is used to acquire images from the same target as the DMUA.

IV. RESULTS

A. Synthetic Aperture Imaging

Two examples of SA imaging with the DMUA are shown to demonstrate its imaging capability. The first is the result of a 3D contrast target in a quality assurance phantom and the second is a tissue mimicking phantom with rib obstacles used in the refocusing experiments described below.

1) *3D Contrast Phantom:* Figure 2 shows grayscale images (50 dB) of an egg-shaped 3D contrast object within the CIRS Model 55 3D contrast phantom. The image on the left was obtained using the DMUA while the one on the right was obtained using the Technos with the CA421 convex probe. The contrast ratio (CR) for the egg-shaped con-

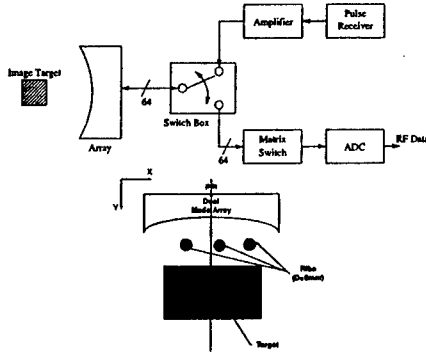


Figure 1: Dual-mode system for lesion and image formation and imaging target with obstacles used in refocusing experiments.

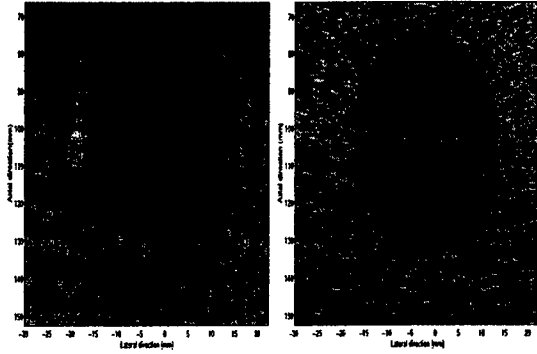


Figure 2: Images (50 dB) from the CIRS Model 55 3D contrast phantom. Left: DMUA w/ GC; Right: Technos.

trast target was computed as follows:

$$CR = 10 * \log_{10} \left(\frac{\sum_{i=1}^{N_r} I_t(i)}{\sum_{i=1}^{N_r} I_c(i)} \right), \quad (4)$$

where $I_c(i)$ [$I_t(i)$] is the average intensity in a $3 \times 3 \text{ mm}^2$ region inside [outside] the contrast target and N_r is the number of regions. The CR value determined from image of DMUA (with gain compensation) and the image from the CA 421 probe are 8.35 dB and 9.12 dB, respectively. These values are quite consistent with the manufacturer specified contrast of 9 ± 0.5 dB. It should be mentioned that, without compensating for intensity gain and element directivity for the DMUA, the contrast ratio would have been 3.3 dB instead of 8.35 dB. It is also interesting to note that the distal edge of the egg-shaped object marks the far end of the 50 dB I_xFOV of the DMUA. One can visually observe the loss of contrast in that region. Spatial and contrast resolution results for various beamforming conditions are shown in [4].

2) *Tissue-Mimicking Phantom with Obstacles*: Figure 3 shows a grayscale image (50 dB) of the phantom shown in

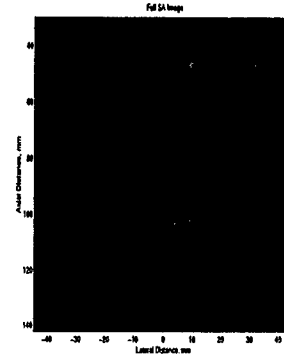


Figure 3: Grayscale image of the tissue-mimicking phantom with ribs shown in Figure 1t acquired using the DMUA in synthetic aperture mode (50 dB).

Figure 1. The image was obtained using the full synthetic aperture technique described in Section II-A. The result is consistent with the schematic with good spatial resolution as well as contrast. In addition to the target and the ribs, the front and back of the tissue-mimicking phantom can be easily discerned (at 80 and 120 mm, respectively). Even though the ribs may be outside the 50 dB I_xFOV of the DMUA, they are sufficiently strong to stand out giving strong specular reflections. Furthermore, the ribs are all spatially registered correctly without distortion.

B. Single-Transmit Focus Imaging

Single-transmit focus imaging can be extremely useful in conjunction with DMUAs in image-guided surgery. By imaging the target tissue using the delay and magnitude profile of the therapeutic beam, it is possible to visualize any strongly scattering structures directly affected by this beam. Figure 4 shows the STF image obtained using a transmit focus at 0 lateral and 100 mm axial (geometric focus). The image is displayed with 40 dB dynamic range and shows that two of the three ribs are visible in addition to the target near the geometric center. This result implies that the transmit focus, when used in therapeutic mode, may cause excessive heating at one or two of the ribs visible on the image.

While the STF image clearly has lower contrast than the full SA image shown in Figure 3, it still shows the target and two of the ribs with good spatial registration. Therefore, it is still useful for identifying targets and potential obstacles as described in the next subsection.

C. Refocusing in the Presence of Obstacles

The image shown in Figure 4 was used to identify the coordinates of the visible ribs as well as define a target point for refocusing within the tissue mimicking phantom. The 40 dB grayscale images shown in Figure 5 show the results of refocusing without (left) and with (right) taking the rib location into consideration. Both of these images were obtained

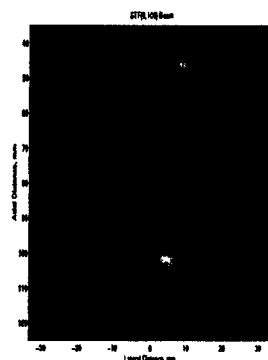


Figure 4: STF image (40 dB) of the target shown in Figure 3. Strong echoes from the three ribs are evident while the needle is less visible.

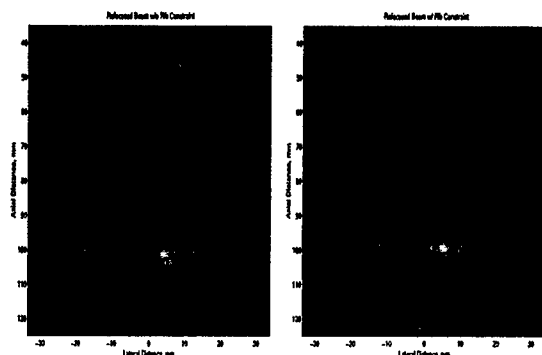


Figure 5: STF images (40 dB) using refocusing without (left) and with (right) taking the critical points are the ribs into consideration.

with a transmit beam focused at the defined target location at 5 mm lateral and 100 mm axial. However, the image on the left was obtained using the algorithm described in Section II-D. One can clearly see the increased visibility of the target compared to the visibility of the ribs. This is due to the reduction of incident power at the ribs as predicted by the weighting algorithm described in Section II-D.

V. DISCUSSION AND CONCLUSIONS

Characterization of the image quality from the DMUA demonstrates the feasibility of using this array in image-guided surgical applications. The spatial and contrast resolutions of this array, while not sufficient for high-quality diagnostic applications, are consistent with the bandwidth and geometry of the array. Furthermore, the speckle components of the beamformed data is suitable for relevant signal processing algorithms such as displacement tracking and temperature estimation.

This paper has also presented the first experimental verification of the feasibility of using image-based refocusing for targeting tissue structures while avoiding critical obstacles

such as the ribs. This may be important if HIFU arrays are to be used for targeting, for example, liver tumors that may be partially obstructed by the rib cage. This result is not to be understood as a form of aberration correction since the refocusing algorithm assumes knowledge of the array directivity at the refocusing target and the critical points. Nonetheless, since these same assumptions are used in beamforming the image in the first place, the algorithm is quite robust against distortions due to inaccuracies in the speed of sound and other tissue properties. The only requirement is that the SA or the STF image used in refocusing provides a recognizable map of the treatment region.

The image quality currently available for DMUAs with image formation techniques described herein may not be sufficient to justify identifying more complex lower scattering critical structures. Furthermore, we are not suggesting that targets such as tumors can be recognized on images provided using the DMUA. However, continued improvement of piezocomposite transducer technologies, especially improved bandwidths of high-power arrays, may bring about sufficient improvement in the image quality to make that possible. In any event, the current image quality may allow for recognizing landmarks on the image that, with the help of more refined imaging systems, can be used in the targeting of tumors and less recognizable tissue structures as they appear on DMUA images.

ACKNOWLEDGMENTS

Funded by Grant DAMD17-01-1-0330 US Army Medical Research and Materiel Command.

VI. REFERENCES

- [1] J. Poorter, C. Wagter, Y. Deene, C. Thomsen, and F. Stahlberg, "Noninvasive MRI thermometry with the proton resonance frequency (PRF) method: In vivo results in human muscle," *Magn. Reson. Med.*, vol. 33, pp. 74–81, 1995.
- [2] P. Meaney, K. Paulsen, A. Hartov, and R. Crane, "Initial in vivo experience with EIT as a thermal estimator during hyperthermia," *Ultrasound Med. Biol.*, vol. 12, pp. 573–591, 1996.
- [3] H. Yao, P. Phukpattaranont, and E. S. Ebbini, "Enhanced lesion visualization in image-guided noninvasive surgery with ultrasound phased arrays," in *Proc. of the 23rd Annual Int. Conf. of the IEEE*, 2001, vol. 3, pp. 2492–2495.
- [4] H. Yao and E. S. Ebbini, "Imaging with large-aperture arrays with heterogeneous directive elements," in *Proc. of the IEEE Ultrasonics Symposium*, 2003, vol. 2, pp. 1243–1246.
- [5] Y. Y. Botros, E. S. Ebbini, and J. L. Volakis, "Two-step hybrid virtual array-ray (var) technique for focusing through the rib cage," *Ultrasonics, Ferroelectrics and Frequency Control, IEEE Trans.*, vol. 45, pp. 989–1000, 1998.
- [6] K. Thomenius, "Evolution of ultrasound beamformers," in *1996 IEEE Ultrasonics Symposium*, 1996, pp. 1615–1622.

APPENDIX 3

REAL-TIME MONITORING OF THE TRANSIENTS OF HIFU-INDUCED LESIONS

Hui Yao and Emad S. Ebbini

Department of Electrical and Computer Engineering
University of Minnesota, Minneapolis, MN 55455

Abstract — RF data from standard B-mode and pulse inversion (PI) imaging of HIFU lesion formation of freshly excised tissue was collected before, during, and after lesion formation experiments in *ex vivo* tissue. Exposures at intensity levels of 1100 W/cm² to 2500 W/cm² for durations of 2, 3, and 5 seconds in a single shot were used. Also continuous raster scan of longer duration (10 - 20 seconds) to form slice or volumetric lesions were monitored. Monitoring was done with a diagnostic scanner and RF data was acquired at 1 frame/second for 60 seconds starting 5 seconds before each shot. Lesion maps from grayscale B-mode and PI images were obtained using level-set methods for each frame and compared with the actual lesion found by inspection. Lesion maps from PI imaging were consistently smaller in size and more in line with the actual lesion size. Transient analysis of harmonic content of lesion echoes show sustained harmonic activity for 10 - 15 seconds after the therapy pulse is turned off (in *ex vivo* liver tissue). A gradual drop in this activity follows with steady state reached within 50 - 60 seconds. It was also shown that the use of short microsecond pulses from the therapy transducer to expose the lesion location during real-time imaging significantly increased the scattering from lesion location.

I. INTRODUCTION

Ultrasound is currently a leading imaging modalities for guidance of numerous interventional procedures. This is due to advantages in cost, portability, ease of integration, and real-time implementation. However, its compromised contrast resolution and poorly understood HIFU lesion dynamics present major obstacles to the goal of mapping these lesions with conventional ultrasound. Over the last few years, several research groups suggested the use of more quantitative techniques such as elastography and remote palpation for mapping HIFU lesions. The successful implementation of these methods relies on better understanding of the transients of the echoes from the HIFU lesion location.

Motivated by P. P. Lele in [1], we hypothesized that this change in echogenicity is due to stable microbubbles that can occur even at low insonation levels. Lele found that subharmonic emission due to microbubbles showed a monotonic increase with intensity from 150 mW/cm² to 1500 W/cm² without a distinct threshold for emission (measurement done *in vitro* and *in vivo* at 2.7 and 1.8 MHz). The

consistency of the increase in echogenicity at the lesion may be explained by the fact that the microbubbles may already be resonant at the imaging frequency (same as the therapeutic HIFU beam).

II. THEORY AND MATHEMATICAL MODELS

A. Level set theory

Reference [2] gives a multi phase level set framework for image segmentation using the Mumford and Shah model for piecewise constant and piecewise smooth optimal approximation. This level set method is especially suitable for HIFU-induced lesion size estimation due to their irregular shape.

Given an observed image u_0 , to find a decomposition Ω_i of Ω and an optimal piecewise smooth approximation u of u_0 such that u varies smoothly inside Ω_i and discontinuously across the boundaries of Ω_i is called the segmentation problem in computer vision [3].

Given u_0 , find (u, C) to minimize

$$\inf_{u, C} \{E^{MS}(u, C)\} \quad (1)$$

where,

$$E^{MS}(u, C) = \int_{\Omega} (u - u_0)^2 dx dy + \mu \int_{\Omega \setminus C} |\nabla u|^2 dx dy + \nu |C| \quad (2)$$

where $\mu, \nu > 0$ are fixed parameters.

A reduced case of the above model is called *minimal partition problem*:

$$E^{MS}(u, C) = \sum_i \int_{\Omega_i} (u - u_0)^2 dx dy + \nu |C| \quad (3)$$

In the piecewise-constant case, two level set functions produce four phases (classes) as shown in Figure 1.

III. EXPERIMENT SETUP

Figure 2 shows a basic experiment setup for the formation of HIFU-induced lesions in freshly excised and degassed porcine livers samples. Experiments were performed with a modified Technos MPX system (ESAOTE SPA, Genoa, Italy) and a therapy transducer (Piezo Technologies, Etalon, Indianapolis, IN). The Technos system was modified to allow imaging in pulse inversion mode in addition to normal

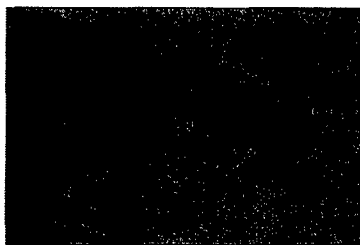


Figure 1: Illustration of two level set functions.

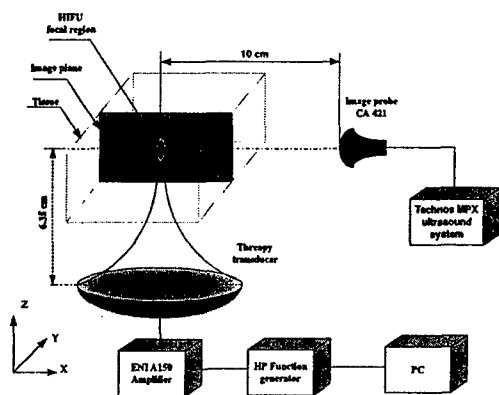


Figure 2: Experiment setup used for HIFU-induced lesion formation using a single element transducer and observation using CA 421 imaging probe monitoring along the axial direction of the lesion.

B-mode imaging. In addition, a hardware module for capturing high quality beamformed RF data allows us to capture and upload up to 60 seconds of full frame data with a specified frame rate. Frame and line trigger signals from the Technos system are also available for synchronizing external events with image acquisition. For this paper, image data were acquired from a CA 421 convex probe in PI mode with a 2-cycle transmit pulse centered at 1.85 MHz. The therapy transducer is a 1.5 MHz single-element spherical-shell transducer with $f_{\#} = 1$ (and focal distance of 63.5 mm.) A HP function generator 33120 A (Hewlett Packard) is connected to the therapy transducer through an ENI Model A150 RF power Amplifier as the HIFU source.

A. Single shot lesion formation

A variety of exposures conditions, before, during, and after lesion formation were tested. RF data from standard B-mode and PI imaging of HIFU lesion formation of freshly excised tissue was obtained. Exposures at intensity levels of 1100 W/cm² to 2500 W/cm² for durations of 2, 3, and 5 seconds in a single shot were used.

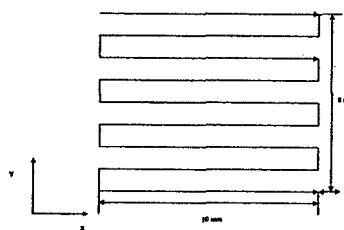


Figure 3: One programmed movement of the phantom holder to form a volumetric lesion.

B. Volumetric lesion formation

Volumetric lesions are formed by moving the tissue holder at a constant speed while the therapeutic beam is on with an intensity suitable for lesion formation. Figure 3 gives one example of a raster scan used in forming a 10 × 8 × 10 mm³ lesion. The translation speed has to be carefully set to produce the desired lesion shape (without over exposure) for a given therapeutic intensity.

C. Imaging with the therapeutic beam

Our previous work on imaging with dual-mode arrays (DMAs) *ex vivo* has shown that the echogenicity of HIFU-induced lesions is consistently higher, even minutes after the lesion has formed [4, 5]. However, the same is not true when monitoring lesions with standard diagnostic imaging transducers. In order to gain a better understanding of this issue, we have designed a synchronized imaging mode with the modified Technos MPX scanner that can be described as follows:

1. The setup of Figure 2 is used.
2. A line trigger signal is obtained from the Technos scanner, which is running at an extremely low mechanical index (MI) in PI mode.
3. On each line trigger, the HP function generator sends a 2 cycle 1.5 MHz sinusoidal pulse with 24 μ s delay through the therapeutic transducer. The pulse from the therapeutic transducer has an extremely low MI as well (0.038 as measured by a calibrated hydrophone). The delay is computed so that scattering from the lesion location registers correctly on the Technos image.
4. The RF data is uploaded and PI images are formed. Since the imaging pulses are so small, almost perfect cancellation of the backscattering is achieved throughout the image. However, since the pulses from the therapeutic transducer have the same polarity for both the positive and negative PI pulses, they add up upon formation of the PI image. Thus, the image contains the angular scattering components from the therapeutic beam.
5. Thirty frames (1 fps) are acquired before lesion

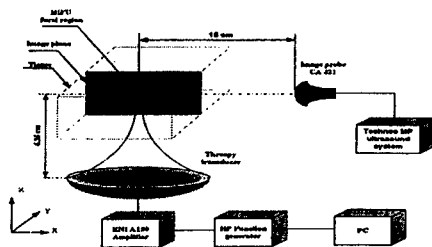


Figure 4: Second harmonic and ultra-harmonic energy as a function of time starting immediately after the therapeutic beam is turned off.

- formation, 15 without and 15 with the pulse from the therapeutic beam.
6. Fifty frames (1 fps) are acquired immediately after lesion formation, 28 without and 22 with the pulse from the therapeutic beam.

This experiment is intended as an approximation of our DMA system. Here we are using the Technos to image scattering from the therapeutic beam at very low intensity and microsecond pulse duration. In the DMA approach, the same thing is done to obtain the backscatter from the therapeutic beam.

IV. RESULTS

A. Transient harmonic content of lesion

Figure 4 illustrate a typical transient analysis result of harmonic content of lesion echoes after the therapy pulse was turned off. The data is typical of an over exposure single-shot lesion (2500 W/cm² for 5 seconds.) Strong harmonic activity appears to persist for 10 - 15 s at the second harmonic ($2 f_0$) and the ultra harmonic ($1.5 f_0$) before decaying to steady state values as can be seen.

B. Lesion mapping

Lesion maps from grayscale B-mode and PI images were obtained using level-set methods for each frame and compared with the actual lesion found by inspection. Figure 5 illustrates volumetric lesion maps from grayscale B-mode and PI images obtained using level-set method. The volumetric lesion was formed by moving the phantom holder at 2 mm/s while maintaining the intensity levels at 2500 W/cm². The lesion size in B-mode images is 172.81 mm², in PI images is 111.19 mm² while the real lesion size is 83.08 mm². Lesion maps from PI imaging were consistently smaller in size and more in line with the actual lesion size. Furthermore, the transient behavior of the lesion maps was easier to observe when the contours were evaluated using the PI images. Please note that the lesion maps given here are meant to define the boundaries of the actual lesion. We simply want to identify the tissue region, as seen on an ultrasound image,



Figure 5: Cross section of a volumetric lesion in *ex vivo* porcine liver: (a) Picture; (b) Lesion map from grayscale B-mode obtained by the level-set method; (c) Lesion map from grayscale PI mode obtained by the level-set method.

that showed a change in echogenicity due to the formation of a lesion by a HIFU beam. Quantitative assessment of irreversible change of tissue due to lesion formation is not an objective of this paper.

C. Imaging with therapeutic beams

Figure 6 demonstrates the value of synchronized imaging with microsecond low MI pulses from the therapeutic transducer as described in Section III-C. The spectrograms (SPGs) show the frequency content of the received RF signal along an A-line through the lesion location. The top SPGs are computed using data in normal B-mode imaging. Figure 6(a), (b), and (c) are SPGs from frames acquired before, 1 s after, and 28 s after lesion formation. One can see a significant increase in harmonic activity after lesion formation, including sub-harmonic activity 1 s after lesion formation. The sub-harmonic component is not visible 28 second after lesion formation. Furthermore, the extent of the region where the harmonic activity occurs is also diminished 28 s after lesion formation. This is consistent with the results from Section IV-A. Figure 6 (d), (e), and (f) are SPGs obtained before, 29 s after, and 51 s after lesion formation, all synchronized with the 2 cycle 1.5 MHz pulses from the therapeutic transducer as described in Section III-C. One can see that the presence of the pulse from the therapeutic transducer before lesion formation only shows as a 1.5 MHz component at the lesion location, but no other nonlinearity is observed. On the other hand, the SPGs 29 and 51 s after lesion formation are very similar in terms of the significant harmonic activity, including sub-harmonic generation. A possible explanation of this result is that even very low MI pulses at the frequency of the therapeutic beam are capable of generating significant harmonic activity at the lesion location. It is possible that microbubbles generated by the HIFU beam still exist well after the transients have died and that even microsecond pulses at their resonance frequency are capable of producing significant increase in both linear and nonlinear scattering from the lesion location.

Figure 7 shows the energy from the lesion location before (bottom) and after (top) lesion formation. The energy is computed from received RF data as described in Section III-

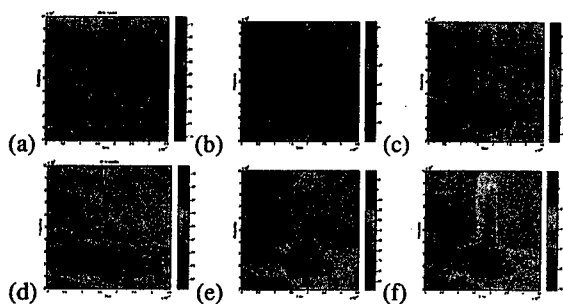


Figure 6: Spectrograms (SPGs) of the RF signal from the center line passing through the lesion. Top: w/o (a) before, (b) 1 s, and (c) 28 s after. Bottom: w/ (d) before, (e) 29 s, and (f) 51 s after.

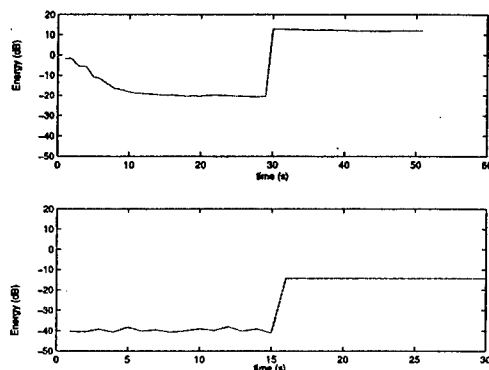


Figure 7: Total energy from the lesion location (a) after lesion formation; (b) before lesion formation. Before the lesion was formed, the therapy beam caused about 25 dB energy increase. The break in the curve corresponds to the introduction of the 2 cycle 1.5 MHz pulse from the therapeutic transducer as described in Section III-C.

C first without and later with the synchronized 2 cycle 1.5 MHz pulses from the therapeutic transducer. Without the insonation using the therapeutic transducer, the energy appears to decay after lesion formation in a similar manner to what we described in Section IV-A. However, once the insonation using the therapeutic transducer begins, a sustained increase in the energy is achieved, 33 dB above the base line in this case. Examining the behavior of the energy before lesion formation, the increase due to the therapeutic beam is only 25 dB. This indicates that the scattering from the lesion location is significantly higher after lesion formation. This is more in line with our previously reported results with the DMA and illustrates the inherent advantage of imaging HIFU induced lesions at the same frequency as the therapeutic beams.

V. CONCLUSIONS

The results presented in this paper show that the increase in echogenicity at the HIFU lesion location can be transient in nature when imaged using standard diagnostic scanners. In addition, the size of the hyperechoic region in B-mode images can vary greatly and may not be well correlated with the actual lesion size in some cases. Quantitative measurements of tissue property that may indicate irreversible tissue damage immediately upon lesion formation is not very likely based on these standard images.

On the other hand, nonlinear (e.g. pulse inversion) imaging techniques consistently provide tighter maps of lesion location on the ultrasound that is typically better correlated with tissue damage. This mode of imaging, in addition to probing the lesion site with the same therapeutic beam (at low MI) may very well provide the tools for addressing this important problem in ultrasound monitoring of HIFU-induced lesions. The results shown herein further support our working hypothesis that imaging HIFU-induced lesions with the therapeutic beam using dual-mode arrays may be a key component in the future of image-guided HIFU systems for noninvasive surgery.

ACKNOWLEDGMENTS

This work was funded by Grant DAMD17-01-1-0330 US Army Medical Research and Materiel Command.

VI. REFERENCES

- [1] P. P. Lele, *Effects of Ultrasound on Solid Mammalian Tissue and Tumors in vivo*, London: Plenum, 1988.
- [2] L.A. Vese and T.F. Chan, "A multiphase level set framework for image segmentation using the mumford and shah model," *Int. Jour. Comp. Vision*, vol. 50, pp. 271–293, 2002.
- [3] D. Mumford and J. Shah, "Optimal approximation by piecewise smooth functions and associated variational problems," *Comm. Pure Appl. Math*, vol. 42, pp. 577–685, 1989.
- [4] Emad S Ebbini, "Combined ultrasound surgery with ultrasound phased arrays," *SPIE Bios: Surgical Applications of Energy*, 1998.
- [5] H. Yao, P. Phukpattaranont, and E. S. Ebbini, "Enhanced lesion visualization in image-guided noninvasive surgery with ultrasound phased arrays," in *Proc. of the 23rd Annual Int. Conf. of the IEEE*, 2001, vol. 3, pp. 2492–2495.